

Coexisting first- and second-order electronic phase transitions in a correlated oxide

K. W. Post^{1,7*}, A. S. McLeod^{1,2,7}, M. Hepting^{1,2}, M. Bluschke^{3,4}, Yifan Wang⁵, G. Cristiani³, G. Logvenov³, A. Charnukha¹, G. X. Ni¹, Padma Radhakrishnan³, M. Minola³, A. Pasupathy², A. V. Boris³, E. Benckiser³, K. A. Dahmen⁶, E. W. Carlson⁵, B. Keimer³ and D. N. Basov^{1,2}

The explanation and control of phase transitions remain cornerstones of contemporary physics. Landau provided an invaluable insight into the thermodynamics of complex systems by formulating their phase transitions in terms of an order parameter. Within this formulation, continuous evolution of the order parameter away from zero classifies the phase transition as second-order, whereas a discontinuous change signals a first-order transition. Here we show that the temperature-tuned insulator-metal transition in the prototypical correlated electron system NdNiO₃ defies this established binary classification. By harnessing a nanoscale optical probe of the local electronic conductivity, we reveal two physically distinct yet concurrent phase transitions in epitaxial NdNiO₃ films. Whereas the sample bulk exhibits a first-order transition between metal and insulator phases, we resolve anomalous nanoscale domain walls in the insulating state that undergo a distinctly continuous insulator-metal transition, with hallmarks of second-order behaviour. We ascribe these domain walls to boundaries between antiferromagnetically ordered domains within the charge ordered bulk. The close correspondence of these observations to predictions from a Landau theory of coupled charge and magnetic orders highlights the importance of coupled order parameters in driving the complex phase transition in NdNiO₃.

The family of rare-earth nickelates (RNiO₃) exemplifies the complexity of correlated electron systems undergoing an insulator-metal transition (IMT)^{1–7}. Experiments affirm the importance of charge ordering, antiferromagnetic ordering, and Mott physics within this system^{8–12}. Thus far, investigations of the IMT in RNiO₃ have primarily relied on area-averaging methods^{8,13,14}, while local aspects of the IMT, known to be important in other correlated oxides^{15–18}, remain obscure in RNiO₃. Clarification of the intrinsic IMT character requires spatially resolving the evolution of the local electronic response across the transition. Accordingly, we examined the nano-infrared (nano-IR) electrodynamics of epitaxial NdNiO₃ films grown on a NdGaO₃ substrate across the IMT with nanometre resolution, using a cryogenically enabled scattering-type scanning near-field optical microscope, detailed in Methods and ref. ¹⁵.

In our local measurements of the optical conductivity, the bulk of the NdNiO₃ film is found to abruptly transition between insulating and metallic end phases without accessing any intermediate state, and can thus be considered archetypically first-order. In contrast to this behaviour, we observe conducting domain walls in a temperature range proximal to the IMT, where optical conductivity evolves continuously from insulating to metallic as the sample is warmed. We argue that these domain walls can be consistently attributed to the spatial boundary across which a secondary coupled order parameter passes between two degenerate equilibrium configurations, thereby triggering a locally second-order IMT. Taking the charge order and antiferromagnetic order as primary and secondary order parameters, while also invoking the unique symmetry relation between their microscopic textures, we construct a detailed Landau

theory that accurately accounts for our observations. Our findings bolster evidence for interacting order parameters in NdNiO₃, while also highlighting the unique capacity of nano-optical methods to uncover hidden electronic phases of correlated oxides.

Results

A schematic of the nano-IR experiment used to access the local optical response of the sample is shown in Fig. 1a, with details described in Methods. Figure 1c presents large-area images of the nano-IR response plotted in the form of the normalized nano-IR scattering amplitude S , also described in Methods. In the false colour scale we employ, blue indicates a weak local signal S corresponding to insulating behavior whereas red indicates stronger S arising from local metallicity^{15,16,19}. Images in Fig. 1c unequivocally show the coexistence of metallic and insulating phases across the IMT of epitaxial NdNiO₃. The insulating phase-fraction associated with images in Fig. 1c is plotted against temperature in Fig. 1b; here the presence of hysteresis reveals a strongly first-order global phase transition, whereas the sharpness of the transition attests to the high quality of the sample. Details of sample growth are provided in Methods.

Several noteworthy real-space features of the IMT in NdNiO₃ are evident within the Fig. 1c images. First, at ambient temperatures, the sample is almost uniformly metallic within the field of view, whereas insulating domains appear below 160 K. These insulating domains expand with decreasing temperature, leaving a persistent metallic ‘ribbon’ within the image, which eventually disappears below 158 K. Second, we note that a small area of these images is occupied by metallic puddles at temperatures as low as 115 K (see Supplementary Information). These sparse puddles serve

¹Physics Department, University of California San Diego, La Jolla, CA, USA. ²Department of Physics, Columbia University, New York, NY, USA. ³Max Planck Institute for Solid State Research, Stuttgart, Germany. ⁴Helmholtz-Zentrum Berlin für Materialien und Energie, Wilhelm-Conrad-Röntgen-Campus BESSY II, Berlin, Germany. ⁵Department of Physics, Purdue University, West Lafayette, IN, USA. ⁶Department of Physics, University of Illinois at Urbana-Champaign, Champaign, IL, USA. ⁷These authors contributed equally: K.W. Post, A.S. McLeod. *e-mail: kpost@lanl.gov

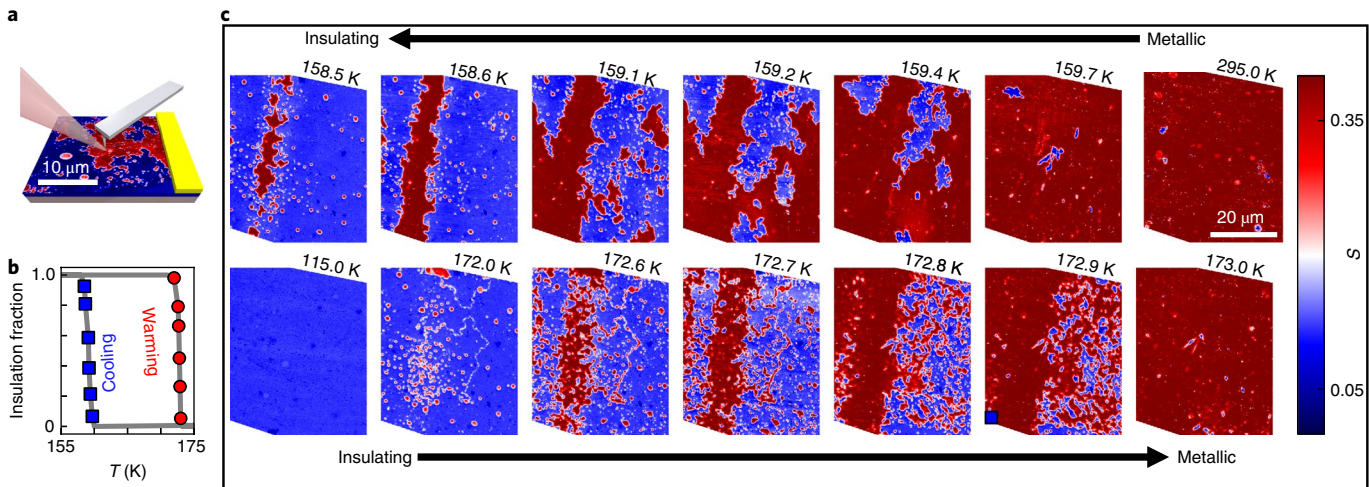


Fig. 1 | Electronic phase separation and percolative phase transition in the NdNiO_3 thin film revealed by nano-infrared imaging. **a**, Schematic of the nano-IR experiment, showing the atomic force microscope cantilever illuminated by an infrared laser at an energy of 100 meV. The yellow bar on the right depicts a gold optical reference structure. **b**, The fraction of pixels within nano-IR images (shown in **c**) that are insulating across the insulator–metal transition (IMT). Thermal hysteresis attests to the overall first-order character of the transition. **c**, Images of normalized nano-IR signal (S) acquired while cooling (top) and warming (bottom) through the IMT. All images were acquired in a co-localized field of view, except for panels at 115 K and 295 K.

as nucleation centres for the metallic phase during the warming transition, and the clusters emerging from these puddles eventually coalesce to form a continuous ribbon, as observed at 172.7 K (left part of the field of view). Upon warming we observe additional novel real-space structures: two narrow and seemingly metallic domain wall structures appearing near $T = 172.0$ K. Crucially, the recurrent enclosed shape of these structures convincingly associates them with boundaries to a hidden underlying domain structure, as we later discuss. These domain walls became more pronounced in the images acquired at 172.6 K and 172.7 K, and are unaffiliated with any topographic features of the sample (see Supplementary Information). Concurrently, additional metallic domains continue to appear and expand at 172.7 K and 172.9 K until the NdNiO_3 sample is almost uniformly metallic at 173.0 K.

For quantitative analysis of the temperature-dependent nano-IR response, a series of images was acquired with an evaporated gold reference structure in the field of view. Using the nano-IR signal of gold (S^{Au}) as a reference, the nano-IR response of the NdNiO_3 (S^{NNO}) could be normalized, line-by-line, to that of gold: $S = S^{\text{NNO}}/S^{\text{Au}}$. Gold-normalized images with approximately equal populations of insulating and metallic regions are shown as insets to Fig. 2a,b. Images of the gold-normalized signal enable representation of the nano-IR response by histograms, with selected data shown in Fig. 2a (Fig. 2b) for cooling (warming). The complete sequence of gold-normalized images and associated histograms are presented in the Supplementary Information, confirming the overall trends shown in Figs. 1,2. It is immediately obvious that distributions of S values on both the cooling and warming IMT are divided between two distinct peaks with mean values of $S^{\text{Ins}} = 0.12$ in the insulating state and $S^{\text{Met}} = 0.35\text{--}0.4$ in the metallic state. Importantly, even at temperatures displaying significant phase coexistence, very few regions exhibit S values residing between these primary values. We may conclude that, even at nanometre spatial scales, the bulk of the sample switches discretely and abruptly between the two end states of the IMT. Consequently, we identify the IMT in NdNiO_3 as a binary, first-order transition that proceeds by nucleation and growth of a minority phase within the parent phase.

Images in Figs. 1,2 provide insight into the roles of short- and long-range interactions in the IMT phenomenology of NdNiO_3 .

Long-range interactions originating, for example, from strain manifest in spontaneous geometric domain texture and characteristic length scales^{15,17,18}. No such repeated textures are identifiable in Figs. 1,2, implying the primacy of short-range or ‘nearest-neighbour’ interactions. This latter point, along with the binary transition revealed by the histograms in Fig. 2, suggests that the domain formation might be interpreted within the framework of an Ising model. An Ising description is suitable for first-order transitions influenced by short-range interactions^{20,21} and proximity to critical points within the global Ising model phase diagram was recently shown to induce real-space features presenting universal power-law scaling behaviours^{21,22}. To evaluate such scaling among the domain morphologies resolved in our measurements, we extracted the radius of gyration (R_ν), a parameter related to the average distance between two points within a given insulator/metal domain, from the characteristic image shown in Fig. 2c. The bi-logarithmic plot of R_ν as a function of the domain area (d) reveals power-law behaviour, remarkably spanning four decades of spatial scales, strongly indicative of Ising universality within this first-order phase transition^{20,21,23}. The power-law behaviour evident in Fig. 2c is described by the exponent $d_\nu = 1.88$, where $R_\nu \propto d^{1/d_\nu}$; a value consistent with the two-dimensional random field Ising model^{20,21}, but further investigations into the universality class of this phase transition are required. Notably, complementary nanoscale photoemission electron microscopy measurements of other NdNiO_3 films found that the IMT morphology reflected stripe-like pinning at surface topographic features²⁴. In contrast, the rich spatial scaling behaviour among domains observed in our NdNiO_3 films suggests that we are probing distinct IMT behaviour governed by isotropic Ising physics unrelated to sample topography. Most importantly, our experimental evidence of Ising behaviour justifies a local Ginzburg–Landau description of the IMT, relevant to our later analysis of the novel behaviour at domain walls.

The binary transition observed in the bulk of the film strongly contrasts with the phenomenology of the metallic domain walls. Within a given thermal cycle of the IMT, the position of each domain wall was found to remain anchored with constant overall size and shape (see Supplementary Information, Supplementary Fig. 2). However, in the course of multiple cycles through the IMT,

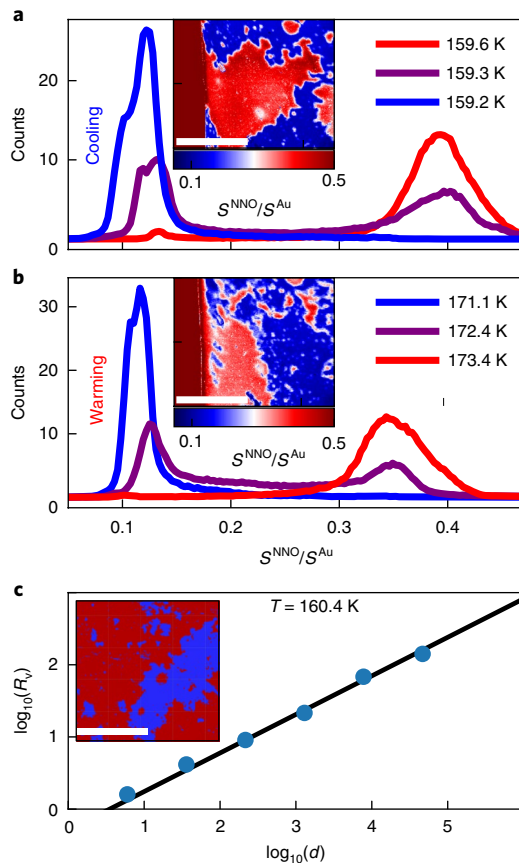


Fig. 2 | Histogram representation of the percolative transition in NdNiO_3 and Ising analysis. **a,b,** Histograms of the normalized nano-IR signal (S) at a subset of temperatures on cooling and warming, with exemplary images in the insets. The gold reference on the left-hand side of the field of view (deep red in insets) enables accurate normalization of the nano-IR signal as described in the text. **c,** The logarithmically binned radius of gyration of insulator and metal domains (R_g) is plotted against the domain area (d), revealing critical scaling; the black line indicates a power-law fit consistent with proximity to a critical point within the two-dimensional Ising model. The inset shows the image at $T=160.4$ K while cooling through the insulator–metal transition, binarized into metal (red) and insulator (blue), from which the scaling curve was extracted. Scale bars in the insets to **a** and **b** indicate $10\ \mu\text{m}$, whereas that in the inset to **c** indicates $20\ \mu\text{m}$.

domain walls emerged at seemingly spontaneous locations, without obvious association with topographic features or sample defects (Supplementary Fig. 5). Moreover, these domain walls appear only while warming through the IMT. To quantify their electronic character, we represent the normalized nano-IR signal measured along domain walls (S^{DW}) via histograms (Fig. 3c). Crucially, S^{DW} grows continuously with increasing temperature from approximately 0.14, characteristic of insulating NdNiO_3 , to approximately 0.35, typical of the metallic state. Figure 3d presents the temperature-dependent optical response of domain walls together with that measured from the rest of the sample; the mean nano-IR response from domain walls (S^{DW} , crosses) should be compared with S^{Ins} (circles) and S^{Met} (squares), all registered within the same field of view at a series of increasing temperatures. Figure 3d shows evidence for the continuous evolution of S^{DW} in sharp contrast to the temperature-independent metallic and insulating optical responses in the bulk of the material. Continuous growth in metallicity along these anomalous domain walls is the hallmark of a second-order phase

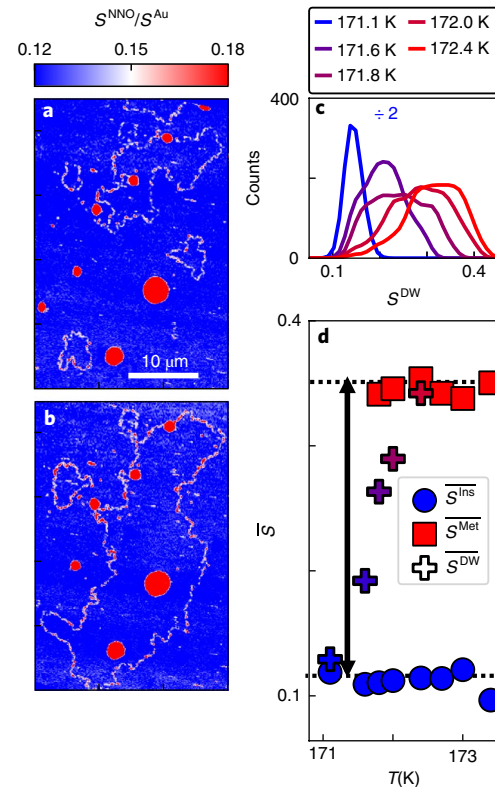


Fig. 3 | Metallic domain walls across the insulator–metal transition. **a,b,** Images at the same spatial location of NdNiO_3 at $T=173.1$ K observed in distinct thermal cycles of the insulator–metal transition. Domain walls appear in these images at spontaneous locations as enclosed lines of enhanced nano-IR response (S), signalling genuine metallic behaviour. **c,** Histograms of the Au-normalized nano-IR response along the domain walls (S^{DW}). **d,** Coloured crosses, blue circles and red squares present the average nano-IR signal within the domain walls (S^{DW}), the insulating domains (S^{Ins}) and metallic domains (S^{Met}), respectively, as a function of temperature. Data presented were extracted from images within the same field of view. Crosses in **d** are coloured to match the corresponding histograms in **c**. The black arrow indicates the range of signal values separating the typical insulating and metallic nano-IR signals in bulk NdNiO_3 .

transition. Therefore, the data in Fig. 3 unveil concurrent first- and second-order transitions occurring throughout the bulk of the film and along seemingly one-dimensional domain walls, respectively.

Cross-sectional profiles of the nano-IR response registered across insulator–metal boundaries and domain walls can provide physical insight into the results shown in Figs. 2,3. Figure 4a presents line profiles associated with averaged cross-sections of a characteristic domain wall (for example, the white arrow in inset; see Supplementary Information for details of data analysis). Inspection of these line profiles reveals a narrow region of metallicity characterized by an enhanced S , growing with increasing temperature, together with an enlarging spatial size as characterized by their full-width at half-maximum (ζ^{DW}) (see Supplementary Information). For comparison, Fig. 4b presents average line profiles typical of the bulk insulator–metal boundaries throughout the rest of the sample. These profiles display remarkably consistent shapes across temperatures spanning the transition, all falling entirely within the thickness of the grey line shown in Fig. 4b. According to the Ising character of the bulk first-order transition (Fig. 2), a Ginzburg–Landau description of these conventional insulator–metal domain boundaries²⁵ predicts a spatial profile with the form $\tanh(x/\zeta^{\text{IMB}})$ along the coordinate normal to the boundary; this form describes our data

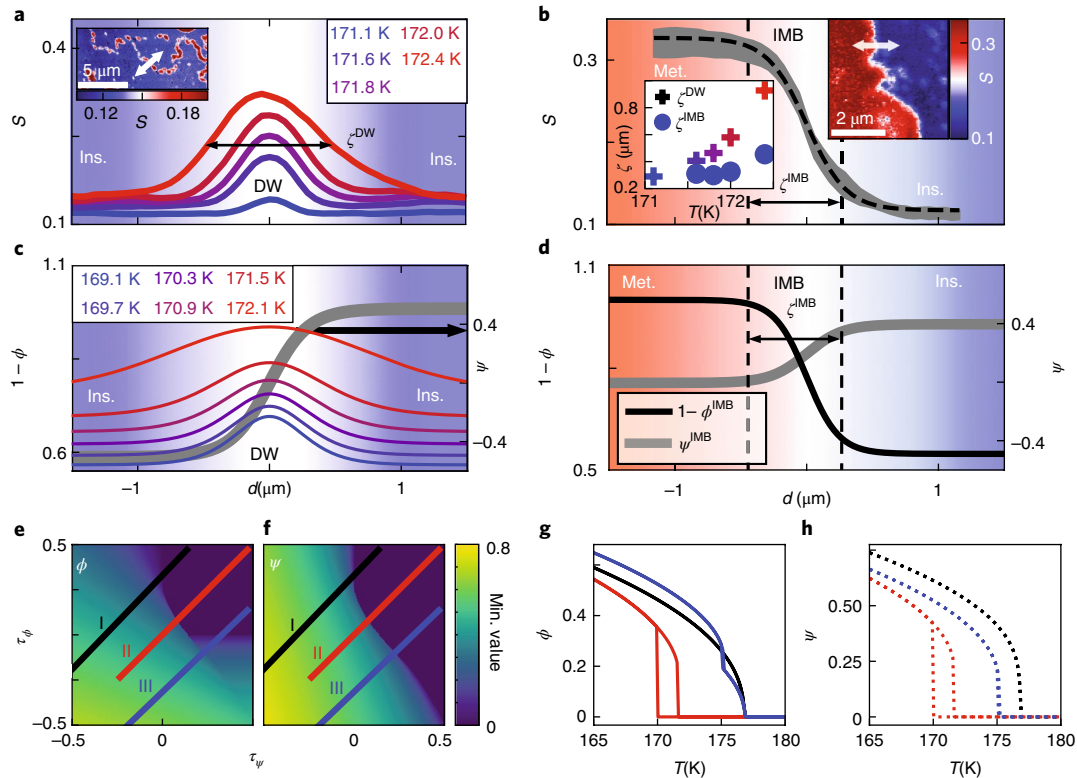


Fig. 4 | Nano-infrared contrast across metal-insulator boundaries. **a**, Spatial profiles of the nano-IR response (S) measured along a path perpendicular (as schematically depicted by the white arrow in the inset image) to a domain wall (DW) at a series of temperatures (coloured); the full-width at half-maximum (ζ^{DW}) of each profile quantifies the DW width. **b**, Characteristic profiles of the nano-IR response measured perpendicular (see top inset) to the insulator–metal boundary (IMB). Multiple IMB profiles recorded over the $T=171.1\text{--}172.4\text{ K}$ range all fall within the grey thickened line. Bottom inset: the typical IMB width ζ^{IMB} (blue circles; see text) compared with ζ^{DW} (coloured crosses) versus temperature. **c**, Predicted profiles of the inverted charge order parameter ($1-\phi$) coupled to an antiphase boundary of a hidden order parameter ψ (grey line and right axis; see text), simulated at increasing temperatures. **d**, Schematically illustrated behaviours of ($1-\phi$) and ψ computed at the IMB for comparison against **c**. The colour backgrounds are used to qualitatively indicate metallic (red) and insulating (blue) portions of the line profiles. **e,f**, Values of order parameters (ϕ and ψ), respectively, that minimize the free energy density of equation (1) as a function of the renormalized temperatures τ_ϕ and τ_ψ . The route by which this phase space is traversed can be tuned by changing the relative ordering temperatures of T_ϕ and T_ψ . Accordingly, we considered three possibilities: $T_\phi=170\text{ K} < T_\psi=177\text{ K}$, $T_\phi=T_\psi=170\text{ K}$ and $T_\phi=177\text{ K} > T_\psi=170\text{ K}$, which lead to the paths indicated by lines I, II and III, respectively. **g,h**, Minimizing values of ϕ and ψ along the three trajectories I,II and III. The hysteresis present in trajectory II indicates the two minimizing values during the first-order phase transition.

well (dashed line in Fig. 4b). Here, the insulator–metal boundary coherence length $\zeta^{\text{IMB}} \approx 300\text{ nm}$ quantifies the stiffness energy of that order parameter associated with the neighbouring insulator/metal domains²⁶. In the lower left inset to Fig. 4b, we compare ζ^{DW} (crosses) and ζ^{IMB} (circles) as a function of temperature, demonstrating that ζ^{IMB} remains virtually constant across the IMT, whereas ζ^{DW} presents a systematic and continuous growth with increasing temperature. Data in Fig. 4b therefore suggest distinct spatial phenomenologies for the IMT at domain walls as compared with the bulk. Taken together with the spontaneity of domain wall locations, this distinction suggests that domain walls might originate from spontaneous symmetry breaking of a hidden order parameter, distinct from the observable order directly associated with the IMT. Moreover, our findings suggest that this hidden order is coupled in some way to the IMT and emerges at a temperature nearly concurrent with the bulk IMT.

Real-space evidence for coupled orders near the IMT

To understand the origin of the domain walls presented in Fig. 3, it is instructive to first consider trends identifiable in the established RNiO_3 phase diagram²⁷. Two undisputed order parameters prevail in the insulating ground state³: unit-cell-doubling charge order with a propagation wavevector $\mathbf{k}_{\text{CO}}=[1/2,1/2,1/2]_{\text{pc}}$, and a unique unit-cell-quadrupling antiferromagnetic texture with wavevector $\mathbf{k}_{\text{AF}}=$

$[1/4,1/4,1/4]_{\text{pc}}$; here we note both in the pseudo-cubic lattice setting. Moreover, there are two distinct routes by which RNiO_3 arrives at this magnetic ground state from the high-temperature metallic phase. For $R=(\text{Nd},\text{Pr})$, the transition occurs through a single first-order transition where antiferromagnetic and charge order emerge simultaneously. For R smaller than Nd, charge order appears at temperatures higher than antiferromagnetic order, and both emerge as second-order transitions⁴. The distinct phase transition phenomenologies associated with these two routes to the same ground state imply that microscopic interplay between antiferromagnetic and charge order might control the classification (first- or second-order) of the IMT.

Coupling between two concurrent or competing order parameters (denoted here by ψ and ϕ) is conventionally represented, to lowest order, by a biquadratic term in the Landau free energy density (F), for example $\psi^2\phi^2$, which has been shown to induce novel behaviour at domain walls²⁸. However, this coupling alone cannot account for the first-order temperature-driven phase transition in $R=(\text{Nd},\text{Pr})$ (see Supplementary Information). Symmetry considerations detailed in refs^{12,29,30} reveal that when two order parameters satisfy the spatial ordering condition $\mathbf{k}_\phi=2\mathbf{k}_\psi$ (as satisfied by charge and antiferromagnetic orders in RNiO_3), a linear–quadratic interaction of the form $\lambda\phi\psi^2$ may be allowed in the free energy expansion. Accordingly, we considered the associated Landau free

energy density previously derived¹² in terms of order parameters ψ and ϕ , and here augmented by spatially dependent gradient ('Ginzburg') terms²⁵:

$$F(\psi, \phi) = \left(\tau_\psi \phi^2 + \phi^4 + \frac{\zeta_\phi^2}{6} (\nabla \phi)^2 \right) + \left(\tau_\psi \psi^2 + \psi^4 + \frac{\zeta_\psi^2}{6} (\nabla \psi)^2 \right) - \lambda \psi^2 \phi \quad (1)$$

where $\tau_j = r_j \frac{T - T_j}{T_j}$ for $j \in \{\phi, \psi\}$ represents the dimensionless temperature controlling each ordering transition. Here r_ϕ and r_ψ are constants, and T_ϕ and T_ψ indicate the bare or uncoupled ordering temperatures for order parameters ϕ and ψ . Interactions between ϕ and ψ are expected to renormalize their physical ordering temperatures, which we denote instead with asterisks by T_ϕ^* and T_ψ^* . Additionally, gradient terms encapsulate short-range Ising-like interactions, reflecting the energy cost of spatial variations in ψ and ϕ that act to align neighbouring regions over characteristic length scales $\zeta_{\phi, \psi}$. Energetic coupling between ψ and ϕ is governed by the coefficient λ , which we generically take as unity in our analysis of the dimensionless Landau theory. Crucially, the presence of this linear-quadratic coupling yields remarkable consequences. The values of ϕ and ψ that minimize the free energy density of equation (1) are presented in Fig. 4e,f as a function of τ_ϕ and τ_ψ . Here, lines labelled I, II and III represent three thermal trajectories through the phase diagrams associated with ϕ and ψ , and the temperature dependence of the coupled order parameters associated with these is presented in Fig. 4g,h, corresponding to three possible scenarios: trajectory I illustrates the case where $T_\phi < T_\psi$; in this case ordering of ψ necessarily induces a simultaneous second-order phase transition in ϕ , so that $T_\phi^* = T_\psi^*$. Alternatively, when $T_\phi = T_\psi$, as illustrated by trajectory II, the phase transition is simultaneously first-order in both order parameters and they emerge discontinuously below $T_\phi^* = T_\psi^*$. Moreover, this first-order behaviour persists over a range of bare critical temperatures for which $T_\phi \approx T_\psi$. Lastly, if $T_\phi > T_\psi$ (trajectory III), the cubic term in equation (1) is inactive and ϕ emerges at T_ϕ in the absence of ψ through a second-order phase transition¹², subsequently followed by the ψ ordering. The phenomenology illustrated by these scenarios is precisely reflected in the established RNiO₃ phase diagram²⁷: the charge order transition is second-order when $T_{\text{CO}} > T_{\text{AP}}$ but becomes first-order only when $T_{\text{CO}} \approx T_{\text{AP}}$. It is thus natural to associate the order parameters ψ and ϕ in equation (1) with antiferromagnetic and charge order, respectively. Lastly, note that 180° phase-slips (for example, antiphase boundaries) of ψ -ordering generate pairwise energetically equivalent equilibrium configurations ($\phi_{\text{eq}}, \psi_{\text{eq}}$) and ($\phi_{\text{eq}}, -\psi_{\text{eq}}$), as accommodated in equation (1), whereas a modified order parameter is expected to interpolate between two such end states³¹. Our subsequent conclusions rely merely on the existence of such energetically degenerate configurations, focusing on the spatial boundaries that emerge between them.

As illustrated in the Supplementary Fig. 7, an antiphase magnetic boundary is physically associated with an inversion of the spin orientation within ferromagnetic planes associated with the spiral antiferromagnetic texture of NdNiO₃^{32,33}. In the one-dimensional case, we have quantified the expected spatial behaviour of charge order $\phi(x)$ close to an antiphase boundary $\psi(x) = -\psi_0 \rightarrow 0 \rightarrow +\psi_0$ by minimizing the global free energy of this system with respect to both $\psi(x)$ and $\phi(x)$ according to equation (1) (see Supplementary Information). Here, x denotes the spatial coordinate perpendicular to the boundary. As we show, the presumption that $\psi(x)$ traverses zero at an intermediate location (labelled $x=0$) ultimately accounts for the gross thermal and spatial dependence of our domain wall observations. The thermal evolution of $\phi(x)$ in such domain wall configurations was reproduced using a model description of our NdNiO₃ sample in which $r_\phi = r_\psi = 8\lambda$, $T_\phi = T_\psi = 170$ K and $\zeta_\phi = \zeta_\psi = \zeta^{\text{IMB}} \approx 300$ nm. First, we note that our nano-IR probe

provides a direct measure for ζ_ϕ via ζ^{IMB} (Fig. 4), and the simplifying assumption that $\zeta_\psi = \zeta_\phi$ is ultimately unimportant to our findings. Second, we reiterate that ψ -ordering triggers ϕ -ordering in this model with simultaneous first-order transitions, thus accounting for the bulk IMT. Lastly, since our experimental probe measures local metallicity, whereas $\phi(x)$ reflects the presumed magnitude of a charge-ordered insulating gap^{11,12}, we expect the quantity $1-\phi$ to show roughly similar trends to our observable nano-IR response S , although the true relationship between these two parameters is probably far more nuanced^{11,34}.

Figure 4c presents line-profiles of $1-\phi(x)$ computed for several temperatures near 170 K in proximity to the domain boundary where $\psi(x=0) = 0$. We also present the calculated lineshape of $\psi(x)$ at 169.1 K (grey line), while calculated lineshapes at additional temperatures approaching the IMT are shown in the Supplementary Information. Profiles of $1-\phi(x)$ grow in both amplitude and width with increasing temperature. Close qualitative agreement with our experimentally acquired line-profiles in Fig. 4a bolsters the conclusion that the observed metallic domain walls arise at locations where the amplitude of a hidden order parameter ψ is suppressed, for example, at magnetic antiphase boundaries. Crucially, continuous evolution of $1-\phi$ demonstrates that equation (1) implies a local second-order charge-ordering phase transition, in accord with the experimental behaviour of S^{DW} . Moreover, domain walls are expected to occur only upon warming within this theoretical scenario. Indeed, the second-order IMT should occur strictly at the 'uncoupled' critical temperature $T_\phi^* \approx 170$ K. Upon cooling, this temperature is fully obscured by hysteresis of the bulk IMT and the ensuing super-cooled metal, in which $\psi = \phi = 0$ (Fig. 1b). However, the metallic domain wall phenomenology presented above demands a ψ -ordered background, characterized by hidden domains in degenerate equilibria, separated by frustrated antiphase boundaries persisting on length scales $\sim \zeta_\psi$, along which $\psi \sim 0$. For comparison, Fig. 4d schematically presents the expected lineshape of both ψ and $1-\phi$ (ref. ²⁵) at a conventional insulator–metal boundary. In this case, both ψ and $1-\phi$ take on roughly temperature-independent $\tanh(x/\zeta)$ lineshapes, similar to that of S presented in Fig. 4b. These results highlight the importance of two order parameters in the IMT of NdNiO₃ while underscoring their respective roles in tuning the first- or second-order character of the transition^{12,30}.

Outlook

Numerous studies have explored the exotic phases emerging when broken symmetries are externally imposed at the interface between distinct oxide materials^{35–38}. However, the boundary between ordered domains within otherwise homogeneous crystalline specimens offers an alternative, yet largely unexplored arena for the observation of exotic phases emerging from broken symmetries³⁹. Apart from surface melting phenomena^{40,41} this is perhaps the first observation of concurrent first- and second-order electronic phase transitions within the same specimen of a solid-state material. Our observations reveal a means of nanoscale control over phase transitions in correlated oxides through manipulation of cooperative order parameters. Future experimental efforts should address the nature of the inferred hidden order and whether it is demonstrably identified as antiferromagnetism, as might be expected from previous characterizations of NdNiO₃. Likewise, further study is needed to elucidate the precise electronic and magnetic nature of observed domain walls, where suppression of a cooperative order parameter may permit exotic and perhaps competing phases to interpolate between the conventional bulk phases⁴². Dichroic X-ray photoemission electron microscopy^{43,44} may enable detection of antiferromagnetic domains in NdNiO₃, as previously accomplished in NiO⁴⁵. However, the spiral magnetic texture of NdNiO₃ may not afford a magnetic linear dichroism detectable by currently available facilities^{5,46}. This technical limitation further motivates the development

and application of complementary imaging techniques sensitive to nano-resolved electronic orders. Nevertheless, the existence of latent nano-scale phases might be a common feature within systems where intertwined degrees of freedom mediate a macroscopic phase transition. Their discovery awaits further nano-resolved imaging investigations.

Methods

Methods, including statements of data availability and any associated accession codes and references, are available at <https://doi.org/10.1038/s41567-018-0201-1>.

Received: 13 November 2017; Accepted: 7 June 2018;
Published online: 9 July 2018

References

- Dagotto, E. Complexity in strongly correlated electronic systems. *Science* **309**, 257–262 (2005).
- Imada, M., Fujimori, A. & Tokura, Y. Metal–insulator transitions. *Rev. Mod. Phys.* **70**, 1039–1263 (1998).
- Medarde, M. L. Structural, magnetic and electronic properties of perovskites (R =rare earth). *J. Phys. Condens. Matter* **9**, 1679–1707 (1997).
- Catalan, G. Progress in perovskite nickelate research. *Phase Transit.* **81**, 729–749 (2008).
- Hepting, M. et al. Tunable charge and spin order in PrNiO_3 thin films and superlattices. *Phys. Rev. Lett.* **113**, 227206 (2014).
- Boris, A. V. et al. Dimensionality control of electronic phase transitions in nickel-oxide superlattices. *Science* **332**, 937–940 (2011).
- Basov, D. N., Averitt, R. D. & Hsieh, D. Towards properties on demand in quantum materials. *Nat. Mater.* **16**, 1077–1088 (2017).
- Stewart, M. K., Liu, J., Kareev, M., Chakhalian, J. & Basov, D. N. Mott physics near the insulator-to-metal transition in NdNiO_3 . *Phys. Rev. Lett.* **107**, 176401 (2011).
- Park, H., Millis, A. J. & Marianetti, C. A. Site-selective Mott transition in rare-earth-element nickelates. *Phys. Rev. Lett.* **109**, 156402 (2012).
- Johnston, S., Mukherjee, A., Elfmov, I., Berciu, M. & Sawatzky, G. A. Charge disproportionation without charge transfer in the rare-earth-element nickelates as a possible mechanism for the metal–insulator transition. *Phys. Rev. Lett.* **112**, 106404 (2014).
- Mandal, B. et al. The driving force for charge ordering in rare earth nickelates. Preprint at <https://arXiv1701.06819> (2017).
- Lee, S., Chen, R. & Balents, L. Landau theory of charge and spin ordering in the nickelates. *Phys. Rev. Lett.* **106**, 016405 (2011).
- Dhaka, R. S. et al. Tuning the metal–insulator transition in NdNiO_3 heterostructures via Fermi surface instability and spin fluctuations. *Phys. Rev. B* **92**, 035127 (2015).
- Ruppen, J. et al. Optical spectroscopy and the nature of the insulating state of rare-earth nickelates. *Phys. Rev. B* **92**, 155145 (2015).
- McLeod, A. S. et al. Nanotextured phase coexistence in the correlated insulator V_2O_3 . *Nat. Phys.* **13**, 80–86 (2017).
- Qazilbash, M. M. et al. Mott transition in VO_2 revealed by infrared spectroscopy and nano-imaging. *Science* **318**, 1750–1753 (2007).
- Liu, M. K. et al. Anisotropic electronic state via spontaneous phase separation in strained vanadium dioxide films. *Phys. Rev. Lett.* **111**, 096602 (2013).
- Liu, M. et al. Symmetry breaking and geometric confinement in VO_2 : Results from a three-dimensional infrared nano-imaging. *Appl. Phys. Lett.* **104**, 121905 (2014).
- Atkin, J. M., Berweger, S., Jones, A. C. & Raschke, M. B. Nano-optical imaging and spectroscopy of order, phases, and domains in complex solids. *Adv. Phys.* **61**, 745–842 (2012).
- Liu, S. et al. Random field driven spatial complexity at the Mott transition in VO_2 . *Phys. Rev. Lett.* **116**, 036401 (2016).
- Phillabaum, B., Carlson, E. W. & Dahmen, K. A. Spatial complexity due to bulk electronic nematicity in a superconducting underdoped cuprate. *Nat. Commun.* **3**, 915 (2012).
- Aharony, A. & Stauffer, D. *Introduction to Percolation Theory* (Taylor & Francis, Abingdon, 2003).
- Perković, O., Dahmen, K. & Sethna, J. P. Avalanches, Barkhausen noise, and plain old criticality. *Phys. Rev. Lett.* **75**, 4528–4531 (1995).
- Mattoni, G. et al. Striped nanoscale phase separation at the metal–insulator transition of heteroepitaxial nickelates. *Nat. Commun.* **7**, 13141 (2016).
- Sanati, M. & Saxena, A. Landau theory of domain walls for one-dimensional asymmetric potentials. *Am. J. Phys.* **71**, 1005–1012 (2003).
- Parks, R. D. *Superconductivity: Part 1* (CRC, Boca Raton, 1969).
- Torrance, J. B., Lacorre, P., Nazzal, A. I., Ansaldi, E. J. & Niedermayer, C. Systematic study of insulator–metal transitions in perovskites $R\text{NiO}_3$ ($R=\text{Pr}, \text{Nd}, \text{Sm}, \text{Eu}$) due to closing of charge-transfer gap. *Phys. Rev. B* **45**, 8209–8212 (1992).
- Darakchiev, M., Catalan, G. & Scott, J. F. Landau theory of domain wall magnetoelectricity. *Phys. Rev. B* **81**, 224118 (2010).
- Lee, S., Chen, R. & Balents, L. Metal–insulator transition in a two-band model for the perovskite nickelates. *Phys. Rev. B* **84**, 165119 (2011).
- Zachar, O., Kivelson, S. A. & Emery, V. J. Landau theory of stripe phases in cuprates and nickelates. *Phys. Rev. B* **57**, 1422–1426 (1998).
- Papanicolaou, N. Antiferromagnetic domain walls. *Phys. Rev. B* **51**, 15062–15073 (1995).
- Scagnoli, V. et al. Role of magnetic and orbital ordering at the metal–insulator transition in NdNiO_3 . *Phys. Rev. B* **73**, 100409(R) (2006).
- Scagnoli, V. et al. Induced noncollinear magnetic order of Nd^{3+} in NdNiO_3 observed by resonant soft x-ray diffraction. *Phys. Rev. B* **77**, 115138 (2008).
- McLeod, A. S. et al. Model for quantitative tip-enhanced spectroscopy and the extraction of nanoscale-resolved optical constants. *Phys. Rev. B* **90**, 085136 (2014).
- Caviglia, A. D. et al. Electric field control of the $\text{LaAlO}_3/\text{SrTiO}_3$ interface ground state. *Nature* **456**, 624–627 (2008).
- Ohtomo, A. & Hwang, H. Y. A high-mobility electron gas at the $\text{LaAlO}_3/\text{SrTiO}_3$ heterointerface. *Nature* **427**, 423–426 (2004).
- Reyren, N. et al. Superconducting interfaces between insulating oxides. *Science* **317**, 1196–1199 (2007).
- Valencia, S. et al. Interface-induced room-temperature multiferroicity in BaTiO_3 . *Nat. Mater.* **10**, 753–758 (2011).
- Ma, E. Y. et al. Mobile metallic domain walls in an all-in-all-out magnetic insulator. *Science* **350**, 538–541 (2015).
- Frenken, J. W. & Van der Veen, J. F. Observation of surface melting. *Phys. Rev. Lett.* **54**, 134–136 (1985).
- Lipowsky, R. Critical surface phenomena at first-order bulk transitions. *Phys. Rev. Lett.* **49**, 1575–1578 (1982).
- Dagotto, E. in *Nanoscale Phase Separation and Colossal Magnetoresistance: The Physics of Manganites and Related Compounds* Ch. 17 (Springer, Berlin Heidelberg, 2013).
- Nolting, F. et al. Direct observation of the alignment of ferromagnetic spins by antiferromagnetic spins. *Nature* **405**, 767–769 (2000).
- Doran, A. et al. Cryogenic PEEM at the Advanced Light Source. *J. Electron Spectrosc. Relat. Phenom.* **185**, 340–346 (2012).
- Scholl, A. et al. Observation of antiferromagnetic domains in epitaxial thin films. *Science* **287**, 1014–1016 (2000).
- Wu, M. et al. Orbital reflectometry of $\text{PrNiO}_3/\text{PrAlO}_3$ superlattices. *Phys. Rev. B* **91**, 195130 (2015).

Acknowledgements

This research was supported by ARO grant W911NF-17-1-0543. Development of cryogenic nano-optical instrumentation is supported by DE-SC0018218 and DE-SC-0012375. D.N.B. is in receipt of the Gordon and Betty Moore Foundation's EPiQS Initiative investigator Grant GBMF4533. E.W.C. and Y.W. acknowledge support from NSF DMR-1508236 and Dept. of Education grant no. P116F140459. Financial support from the Deutsche Forschungsgemeinschaft (DFG) under Grant No. SFB/TRR80 G1 is acknowledged by M.H., M.B., G.C., G.L., P.R., M.M., E.B. and B.K.

Author contributions

K.W.P., A.S.M and D.N.B. conceived of and conducted the nano-IR experiments, analysed the data, and composed the article. A.C., G.X.N. and A.P. assisted with nano-IR measurements. M.H., M.B., G.C., G.L., P.R., M.M., A.V.B., E.B. and B.K. grew the NdNiO_3 film and conducted the XRD and transport measurements. Y.F.W., K.A.D. and E.W.C. performed theoretical studies to interpret domain morphology data in the context of Ising models and Landau theory.

Additional information

Supplementary information is available for this paper at <https://doi.org/10.1038/s41567-018-0201-1>.

Reprints and permissions information is available at www.nature.com/reprints.

Correspondence and requests for materials should be addressed to K.W.P.

Publisher's note: Springer Nature remains neutral with regard to jurisdictional claims in published maps and institutional affiliations.

Methods

Nano-infrared imaging. A schematic of the nano-optical imaging set-up is shown in Fig. 1a. Focused infrared light is incident upon and scattered from the metallic tip of an atomic force microscope (AFM) probe (SCM-PTSI, Bruker Nano) oscillating at a frequency $\sim 75\text{ kHz}$ near the sample surface while the microscope is operated in amplitude modulation AFM feedback. The back-scattered radiation from the probe encodes information about the optical permittivity of the sample at the frequency of the laser source. Back-scattered radiation is registered by a liquid nitrogen-cooled mercury cadmium telluride photodetector and resolved from the background through Michelson interferometry in a pseudo-heterodyne detection scheme. To the first approximation, the amplitude of back-scattered radiation modulated at high harmonics ($n \geq 2$) of the cantilever oscillation frequency provides a measure of the local near-field optical response of the sample and, by implication, its optical conductivity resolved at the 20-nm scale^{15,47}. Throughout this work, we utilized this nanoscale optical probe to evaluate the low-energy ($\omega = 900\text{ cm}^{-1}$) optical response associated with free carriers (Drude conductivity) in the metallic state of the NdNiO₃ film, or alternatively the bulk energy gap of the insulating state.

Growth of the NdNiO₃ film. The 7 nm thin film was grown by pulsed-laser deposition from a stoichiometric target of NdNiO₃ on a NdGaO₃ single-crystalline substrate using a KrF excimer laser with a 2 Hz pulse rate and a 1.6 J cm^{-2} energy density. A LaAlO₃ capping layer of approximately 1.5 nm thickness was grown at the end of the growth process. All materials were deposited in a 0.5 mbar oxygen atmosphere at 730°C and the capped film was subsequently annealed in a 1 bar oxygen atmosphere at 690°C for 30 min. Structural and electronic characterization of these samples is detailed in the Supplementary Information.

Data availability. The data that support the plots within this paper, and other findings of this study are available from the corresponding author upon reasonable request.

References

47. Fei, Z. et al. Electronic and plasmonic phenomena at graphene grain boundaries. *Nat. Nanotech.* **8**, 821–825 (2013).